Topologically-protected interior for three-dimensional confluent cellular collectives

Tao Zhang [1,*] and J. M. Schwarz [2,3,†]

[1] *Department of Polymer Science and Engineering, Shanghai Jiao Tong University, Shanghai 200240, China*

[2] *Physics Department, Syracuse University, Syracuse, New York 13244, USA*

[3] *Indian Creek Farm, Ithaca, New York 14850, USA*

(Received 14 June 2022; accepted 13 October 2022; published 29 November 2022)

Organoids are *in vitro* cellular collectives from which, for example, brain-like, or gut-like, or kidney-like structures emerge. To make quantitative predictions regarding the morphology and rheology of a cellular collective in its initial stages of development, we construct and study a three-dimensional vertex model. In such a model, the cells are represented as deformable polyhedrons with cells sharing faces such that there are no gaps between them, otherwise known as confluent. In a bulk model with periodic boundary conditions, we find a rigidity transition as a function of the target cell shape index s_0 with a critical value $s_0^* = 5.39 \pm 0.01$. For a confluent cellular collective with a finite boundary, and in the presence of lateral extensile and in-plane, radial extensile deformations, we find a significant boundary-bulk effect that is one-cell layer thick. More specifically, for lateral extensile deformations, the cells in the bulk are much less aligned with the direction of the lateral deformation than the cells at the boundary. For in-plane, radial deformations, the cells in the bulk exhibit much less reorientation perpendicular to the radial direction than the cells at the boundary. In other words, for both deformations, the bulk, interior cells are topologically protected from the deformations, at least over time scales much slower than the timescale for cellular rearrangements and up to reasonable amounts of strain. Our results provide an underlying mechanism for some observed cell shape patterning in organoids and in *in vivo* settings. Finally, we discuss the use of a cellular-based approach to designing organoids with new types of morphologies to study the intricate relationship between structure and function at the multicellular scale.

DOI: 10.1103/PhysRevResearch.4.043148

I. INTRODUCTION

Organoids provide us with an *in vitro* window into organogenesis [1,2]. An organoid typically starts off as a cellular collective (a clump of cells) consisting of stem cells. The cells are given some induction medium to help them differentiate into either neurons or kidney cells or heart muscle cells, for instance. The cellular collective is then transferred to a petri dish containing Matrigel, which contains collagen as well as growth factors and morphogens, followed by additional protocol, such as agitation [3,4]. Even at the initial stages, there is some patterning of the collective in terms of cell shape [5]. Over a longer time scale, as the cells divide, the organoid continues to develop additional structure and a brain organoid [6], for example, ultimately emerges. Intriguingly, brain organoids, exhibit the *in vivo* phenomenon of neuronal diversity [7]. Additionally, at even later stages of development, neurons in the brain organoid begin to fire and fire synchronously, just as in the developing brain [8]. Intestinal organoids, on the other hand, self-assemble into crypt-villus units [9]. In addition to providing a window into organogenesis, organoids also provide an intermediary platform between cells and organs to study disease [1,2]. For instance, scientists are currently exploring how SARS-CoV-2 infects the brain via brain organoid studies to provide guidance for drug treatment of COVID-19 [10,11].

We hone in on the early stages of organoid development. In particular, for quasi-two-dimensional geometries, which are used in the formation of brain organoids [5] and intestinal organoids [12] there appears to be differences in cellular structure between the cells in contact with the Matrigel at the edge of the organoid and the cells in the bulk (or interior). In particular, the cells on the boundary appear to be more elongated with the direction perpendicular to the edge of the Matrigel. The cells in the bulk, on the other hand, appear to be more globular with no apparent, particular orientation [5]. For three-dimensional geometries, a central hole, or lumen, in place of a bulk of globular cells can emerge [6].

Given the apparent ubiquity of the phenomenon, we ask: How does such a topologically-protected interior in these cellular collectives arise? Theoretical work has been done to demonstrate how an individual versus multiple cortex-core structures materialize from a hydrodynamic description of active forces in cellular collectives to help regulate the overall brain organoid architecture [13]. Here, we implement a cellular-based computational approach to probe the above question, namely, a three-dimensional vertex model [14–18]. Such models are ones with cells represented as deformable polyhedrons and there are no gaps between them. While two-

*zhangtao.scholar@sjtu.edu.cn

†jmschw02@syr.edu

dimensional vertex models have been studied widely [19–28], three-dimensional vertex models have not been studied as extensively. Presumably, this is, in part, because there is no publicly available code, while two-dimensional codes, such as CHASTE [29,30], CellGPU [31], and the different, but related, active vertex model [32], are available.

As for prior three-dimensional vertex model work that has been done, researchers have found that introducing polarized interfacial tension allows for cells to migrate individually, or even as a cluster, through a tissue [33]. In addition, studies of branching in tissue to form a lung have also been explored in such models [34]. And yet, prior studies of the three-dimensional vertex model have focused on a particular energy functional that is different from a three-dimensional extension of the two-dimensional energy functional in which a rigidity transition was uncovered [23] and with support from experimental observations of asthmatic bronchial epithelial tissue [35]. More recently, the same two-dimensional vertex model extended to include two cell types predicted a new micro demixing phenomenon, which was supported by experiments [26]. We will use the same version of the energy functional as the one exhibiting a density-independent rigidity transition in two dimensions to ask first whether or not there exists a rigidity transition in a bulk model. Prior work has demonstrated that there exists a rigidity transition in a three-dimensional Voronoi model as a function of the three-dimensional shape index [36]. We will then explore how deformations of a confluent cellular collective affect the morphology and the rheology of the collective. Our efforts represent a substantive leap from earlier, elegant work studying the shapes of shells composed of the polyhedrons as we now can probe the interior [37].

II. MODEL

Cells are biomechanical and biochemical constructs that are not in equilibrium, i.e., they are driven by internal, or active forces. The biomechanics of the cellular collective is given by the energy functional

$$E = K_V \sum_j (V_j - V_0)^2 + K_A \sum_j (A_j - A_0)^2 + \gamma \sum_\alpha \delta_{\alpha,B} A_\alpha, \tag{1}$$

where A_j denotes the jth cell total area, the jth cell volume is denoted by V_j, and α labels the faces of the cells, with $\delta_{\alpha,B} = 0$ if a face is not at the boundary B of the collective and 1 otherwise. Given the quadratic penalty from deviating from a cell's preferred volume V_0 and area A_0, K_V and K_A are volume and area stiffnesses, respectively. Physically, the volume term represents the bulk elasticity of the cell with V_0 denoting a target volume. The area term for cell j can be rewritten as $K_A A_j^2 + \Gamma A_j + \text{const.}$, where $\Gamma = -2K_A A_0$. Here the first term $K_A A_j^2$ represents the contractility of the actomyosin cortex, and the second term ΓA_j represents an interfacial tension Γ set by a competition between the cell-cell adhesion at negative Γ (larger A_0) and the cortical contractility at positive Γ (smaller A_0). Indeed, cell-cell adhesion and contractility are coupled [38]. For instance, knocking out E-cadherin in keratinocytes, effectively changes the contractility [26]. We can tune for cell-cell adhesion through the target area A_0. The target area A_0 has a physical meaning of controlling whether the cell-cell adhesion or the cortical tension dominates. This translation from the mathematics to the biology is a generalization from prior translations for two-dimensional models in which the effective target perimeter P_0 (assuming $A_0 = 1$) translates to a competition between cell-cell adhesion at larger P_0 and contractility at smaller P_0. Note that the target area A_0 is also related to the isotropy of cortical contractility. The larger the A_0, the less isotropically contractile the cell is, and vice versa. The less isotropically contractile a cell is, the more likely it can develop contractility in a particular direction, or anisotropic contractility as modulated by stress fibers, for example [39]. As for the linear area term, the cells at the boundary of the cellular collective, there is an additional surface tension term for faces interacting with the "vacuum". One can nondimensionalize any length l in the simulation with $l = V_0^{1/3}$. An important parameter in these models is the dimensionless shape index $s_{0,j} = A_{0,j}/(V_{0,j})^{2/3}$. A regular tetrahedron has a dimensionless shape index of $s_0 \approx 7.2$, for example.

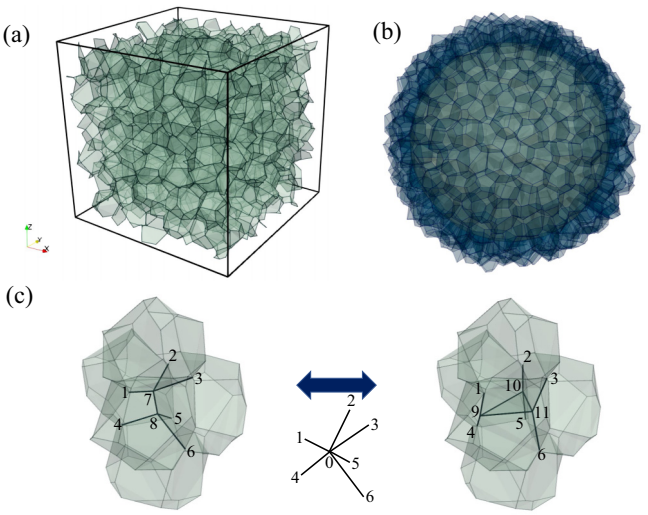

FIG. 1. 3D vertex model. (a) Snapshot of the bulk model with $s_0 = 5.60$. (b) Snapshot of the cellular collective (light green) with $s_0 = 5.60$ and empty cells (dark green). (c) Snapshot series of a reconnection event between cells in which the edge composed of the vertices labeled 7 and 8 becomes the triangle composed of vertices labeled 9, 10, and 11, and vice versa to result in a change of neighbors while remaining confluent. The numbers indicate serial vertices, and solid lines indicate edges. The point labeled 0 indicates the center of the reconnection event.

Now that we have addressed the biomechanical aspect of cells. We must also account for their dynamics. Cells can move past each other even while the tissue remains confluent. In two dimensions such movements are known as T1 events. Understanding such events are key to understanding the rigidity transition in two dimensions [23]. In three dimensions, such movements are known as reconnection events. As for how cells exchange neighbors via a reconnection event, following Okuda and collaborators [40], we focus on edges going to triangles and vice versa. See Fig. 1(c). To determine if a reconnection event occurs, we look for edges with lengths

less than l_{th} and triangles with all three edge lengths less than l_{th}. If there are indeed such edges or triangles, we choose one of the edges randomly and perform an edge-to-triangle reconnection event in which the edge vanishes and is replaced by a triangle whose normal vector is parallel to the initial edge, or choose one of the triangles randomly and perform a triangle-to-edge reconnection event, should the following conditions introduced in the paper of Okuda and collaborators [40] be met to ensure whether or not a reconnection event is physically plausible. The *first condition* is that the change in energy before and after the reconnection event should be in the order of l_{th}. The *second condition* relates to resolving the topological irreversibility and satisfies the following subconditions: (1) two edges do not share two vertices simultaneously, (2) two polygonal faces do not share two or more edges simultaneously, and (3) two polyhedral cells do not share two or more polygonal faces simultaneously. The third subcondition is implemented given the computational efficiency and was not discussed explicitly in the paper of Okuda and collaborators [40].

After every ten time steps in the MD simulation are completed, all the edges and triangles that can undergo a reconnection event, given the above conditions, are tagged. First, reconnection events from edge to triangle are performed sequentially. Second, reconnection events from triangle to edge are performed sequentially. We allow for the possibility that some edges and triangles initially tagged can become untagged as the reconnection events occur. Edges and triangles are only subtracted from the tagged list and not added to it.

In addition to reconnection events, there is an underlying Brownian dynamics for each vertex. Specifically, the equation of motion for the position $\mathbf{r}_I$ of a single vertex I is

$$\dot{\mathbf{r}}_I = \mu \mathbf{F}_I + \mu \mathbf{F}_I^B, \tag{2}$$

with $\mathbf{F}_I$ and $\mathbf{F}_I^B$ denoting the conservative force and the random thermal force on the Ith vertex respectively. The force $\mathbf{F}_I$ is determined from both the area and volume energetic constraints and, hence, includes cell-cell interactions. In addition, each Ith vertex performs a random walk with an effective diffusion coefficient of $\mu k_B T$, where T is an effective temperature. Unless otherwise specified, the mobility $\mu = 1$. Finally, the Euler-Murayama integration method is used to update the position of each vertex. See Table I for the listing of the parameters used in the simulations and their corresponding values.

As for bulk case simulations, an initial state is created using a three-dimensional Voronoi tessellation [41] given randomized cell centers and assuming periodic boundary conditions. The vertices, edges, and faces of each cell are then defined. To compute the force on each vertex due to the energetic contributions in Eq. (1), each polygonal face that has four or more edges is broken up into radially arranged triangles composed of each edge and the center point of the polygonal face [40]. The pressure of each cell due to the volume term and the tension of each triangular face due to the area term in Eq. (1) are computed. The force on each triangular face is determined by multiplying the pressure with the surface area and multiplying the tension with the edge length. This force is then redistributed to the vertices making up each face. This method was implemented, as opposed to computing the partial derivatives $\mathbf{F}_I = \nabla_I E$ of the energy E with respect to the positions of the Ith vertex given the computational efficiency of this latter method and have checked that the two calculations are equivalent. Once the forces are known, the positions of the vertices are updated using Eq. (2) that includes a random thermal force $\mathbf{F}_I^B$. The simulation timestep is referred to as $d\tau$. The system is equilibrated for a time period $\Delta t = 10\,000$ before collecting data for the overlap function plots.

TABLE I. Table of the parameters used in the simulations.

Diffusion constant	D	1
Thermal energy	$k_B T$	10^{-4}
Simulation timestep	$d\tau$	0.005
Cell area stiffness	K_A	1
Cell volume stiffness	K_V	10
Cell target volume	V_0	1
Cell target surface area	s_0	5.0–5.8
Boundary cell surface tension stiffness	γ	1
Boundary cell extension speed	v	10^{-4}
Reconnection event threshold edge length	l_{th}	0.02
Number of bulk cells	N_B	512
Number of cellular collective cells	N	400
Damping	ξ	1
Number of realizations	N_R	20
Maximum strain of lateral extension	ϵ_l	108%
Maximum strain of radial extension	ϵ_r	52%
Long axis sample length after lateral extension	L_l	20
In-plane sample diameter after radial extension	L_r	14

To explore the properties of a cellular collective, one must consider boundaries. For instance, as cellular collectives become embedded in Matrigel to ultimately become organoids, they interact with the deformable Matrigel as they develop [6]. Here, we do not explicitly consider Matrigel, though prior work in two dimensions of a cellular collective embedded in a spring network has been done [42]. Instead, we construct a confluent cellular collective, or a clump of confluent cells, by making a spherical cut-out of the bulk periodic system that contains cells with empty cells beyond the boundary between cells and empty space [see Figs. 1(a) and 1(b)] as has been done in two dimensions [42]. For those cells at the boundary of the clump, the interfacial vertices contain an additional interfacial surface tension γ. Moreover, we allow reconnection events with more than one empty, or phantom, cells.

Finally, we explore the rheological properties of the three-dimensional vertex model in bulk as well as the confluent cellular collective. For the latter, we consider deformations on the cellular collective on the boundary by having the boundary vertices undergo constant speed v outward. In other words, a constant extensile strain/deformation rate is imposed. In terms of direction, we explore two kinds of extensile strain, one that is uniaxial and one that is in-plane, radial. One can readily interpret the deformation as an external one, or one that is applied to the clump. Alternatively, one can interpret the deformation as an internal one due to, for example, leader cells whose polymerization of the cytoskeleton is in an outward direction much like a flexocytes model with internal structure [43]. Finally, these boundary vertices do not exhibit thermal-like fluctuations in their motion.

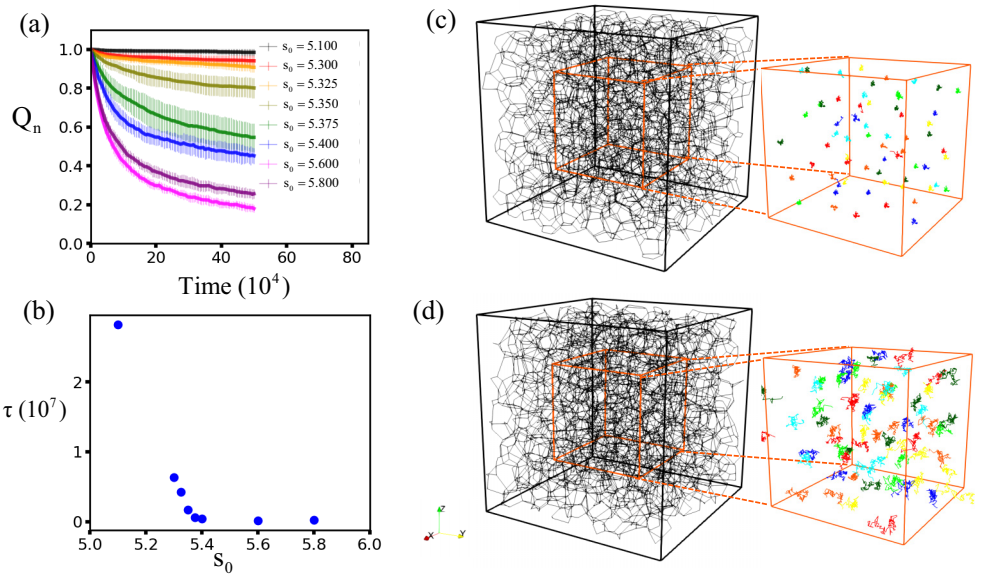

FIG. 2. Existence of a rigidity transition in the bulk model. (a) Overlap function Q for different values of s_0. (b) Floppy-rigid boundary: decay time τ as a function of s_0. [(c),(d)] Trajectories of vertices initially located within the center cubic box with size 4.0 over a time period $\Delta t = 400\,000$ for $s_0 = 5.3, 5.6$, respectively.

III. RESULTS

A. A rigidity transition in bulk

Prior studies have found a density-independent phase transition in two-dimensional vertex models as well as a three-dimensional Voronoi model with the same form of the energy functional [23,36]. Is there then a similar transition in the three-dimensional vertex model presented here? To determine whether or not there is a transition, one can look at energy barriers to neighbor exchanges. In this approach, one can determine a necessary condition for cellular rearrangement in two dimensions. For cells with area set to unity, for example, having a target shape index that is regular pentagon involves no energy cost for 4-point vertex to emerge—the geometry at which the cells perform a neighbor swap. Alternatively, one can measure the shear modulus of the system [23,36]. Since we are implementing a dynamical approach, with each vertex undergoing Brownian motion in a many-body, cell-cell interaction potential, one can also determine whether or not the system is a fluid or solid by looking at the mean-squared displacement of cells. However, it is sometimes difficult to pinpoint the transition point given that the crossover time to a caging can be rather long [24].

Instead, we use the concept of a neighbors-overlap function, combined with trajectories, to determine whether the cells remain localized or not [44]. In particular, Q_n is defined as

$$Q_n(t) = \frac{1}{N}\sum_{j=1}^{N} w_j, \tag{3}$$

where N is the number of cells, $w_j = 0$ if cell j has lost two or more neighbors and $w_j = 1$ otherwise. Should the system be solid-like and so the cells do not change neighbors, then $Q_n(t) = 1$. Should the system become more fluid-like and so cells do change neighbors, then $Q_n(t) < 1$. The smaller $Q_n(t)$ becomes, the more cells change neighbors. We must also couple this measurement with observations of the trajectories of cells since the changing of neighbors could result in some localized movement, i.e., caging, as opposed to system-spanning trajectories, which are indicative of something more akin to a fluid, as opposed to a glassy state. Note that we have not yet incorporated a mechanism to prevent back-and-forth reconnection events. Recent work implements such a mechanism in two dimensions [45,46] .

We measure $Q_n(t)$ for the bulk system for different target shape parameters, averaging over 20 realizations. See Fig. 2(a). We observe that for $s_0 = 5.1$, $Q_n(t) = 1$ and remains at unity throughout the duration of simulation on average. However, for $s_0 = 5.8$, it is clear that $Q_n(t)$ is decaying to a value less than unity. The overlap function is fit to an exponential decay with τ_n defined as the decay time. In Fig. 2(b), we plot the decay time τ_n as a function of s_0. We find that τ_n approximates zero around $s_0^* = 5.39 \pm 0.01$, which is an estimate for the rigidity transition point since the typical time scale for cellular rearrangements becomes zero. Additionally, some cell trajectories are plotted in Figs. 2(c) and 2(d). Some trajectories span larger than one cell length, for the larger s_0, to indicate that the cells are not caged, at least on that scale, and so not simply switching back and forth between neighbors. We, therefore, find that both solid-like and fluid-like behaviors as a function of s_0, suggesting a density-independent rigidity transition in this three-dimensional vertex model. We also study the cell shape index distribution to find that for $s_0 = 5.40$ and above the average of the distribution tracks the target s_0 indicating that cells can achieve their target shape while in the fluid-like state, while in the solid-like state, the average of the distribution cannot track the target s_0 and the distribution is more broaden than the fluid-like state (see Fig. S1 within the Supplemental Material [47]). We note that

if we extend the definition of w_j to be $w_j = 0$ if cell j has lost N_l or more neighbors and $w_j = 1$ otherwise, where $N_l = 3, 4$, the rigidity transition point remains unchanged (see Fig. S2 within the Supplemental Material [47]).

B. Boundary-bulk morphology with lateral extensile strain

While understanding additional bulk behavior in three dimensions is important, we now focus on a confluent cellular collective, or a clump of cells. As discussed above, we take the initial Voronoi construction (based on randomized points in three dimensions) and then carve out a cluster of cells such that any polyhedron that is not part of the cellular collective is simply empty space. The faces of cells in contact with empty have an extra energetic interfacial surface area contribution.

To explore the structure and rheology of the cellular collective as it undergoes a deformation, we assign the vertices in contact with "empty space" a deterministic velocity v outward along a particular, uniaxial direction. As these vertices move outward, the structure of the cellular collective adjusts so that the collective remains confluent. Moreover, we explore whether or not a collective that begins as a solid with $s_0 = 5.0$ and then becomes a fluid as a result of the deformation. In other words, how do deformations affect the rheology of the cellular collective?

As for the structure of the cellular collective following the uniaxial, extensile deformation, we ask whether or not cells align along the uniaxial direction of extension. Prior studies of epithelial colonies that are uniaxially pulled are able to identify topological defects within a nematic background [48]. Such defects are recapitulated by a two-dimensional vertex model with additional polarization terms added to energy functional to account for polarization, and nematic ordering is present even before the pulling [48]. While we do not observe nematic ordering before the uniaxial, extensile deformation, we ask whether or not there exists emergent nematic ordering along the uniaxial direction. To test for this, we fit each polyhedron to a minimal volume ellipsoid and then determine the orientation of the long axis, dub it a "rod", and compute the average of the absolute value of the cosine of the angle between any two rods for any pair of rods (i, j) some distance between the two centers $r_{ij} \leqslant \Delta r$, or

$$C(\Delta r) = \frac{1}{M} \sum_{r_{ij} \leqslant \Delta r} \frac{|\vec{d}(\mathbf{r}) \cdot \vec{d}(\mathbf{r} + r_{ij}\mathbf{n})|}{|\vec{d}(\mathbf{r})||\vec{d}(\mathbf{r} + r_{ij}\mathbf{n})|}, \tag{4}$$

where M is the number of pairs, $\mathbf{n}$ is the three-dimensional unit vector, and $\vec{d}$ is the vector aligned with the rod to represent the rod orientation. The correlation function $C(\Delta r)$ indicates the correlation in orientation between two rods with the centers a distance $r \leqslant \Delta r$ from each other.

Since the vertices on the edge of the cell collective are different from the bulk cells in that there is an extra energetic contribution, we separate out the boundary cells from the bulk cells and look for correlation in alignment between cells in the bulk and between cells on the boundary, see Fig. 3. For $s_0 = 5.6$, we find that for bulk cells, the spatial correlation in alignment is rather similar to the bulk system with periodic boundary conditions (see Fig. S3 within the Supplemental Material [47]). In other words, we do not observe nematic ordering. The boundary cells, however, do exhibit ordering with a much higher correlation in alignment as compared to the bulk cells. Intriguingly, the drop in alignment correlation from the boundary to the bulk is significant given that the boundary is only one-cell layer thick. See Fig. S4 within the Supplemental Material [47] for the plots of $C(\Delta r)$ for the outermost layers and the second outermost layer for additional support of this statement. In other words, there is a one-cell skin depth phenomenon in which the boundary cells align with the deformation, but the bulk cells do not (see Movie S1 within the Supplemental Material [47]). While this may not be unexpected for a fluid-like system, this difference emerges in the solid-like system with $s_0 = 5.0$ as well, however, the difference in spatial correlation in alignment amongst cells in the bulk and amongst cells in the boundary, is not as large. Presumably, this trend is because there are fewer reconnection events in the solid-like phase, so the system overall is less plastic in the presence of the deformation and, therefore, less responsive to the deformation. See Fig. S5 within the Supplemental Material [47] for the plots of the distribution of the aspect ratio of boundary/bulk cells for additional support of this one-cell skin depth phenomenon. During the lateral extension, the boundary cells undergo much more aspect ratio change than the bulk cells in both fluid-like and solid-like systems, showing that the boundary cells can mechanically protect the interior.

What is the mechanism driving this one-cell layer skin depth phenomenon? Earlier two-dimensional studies found a

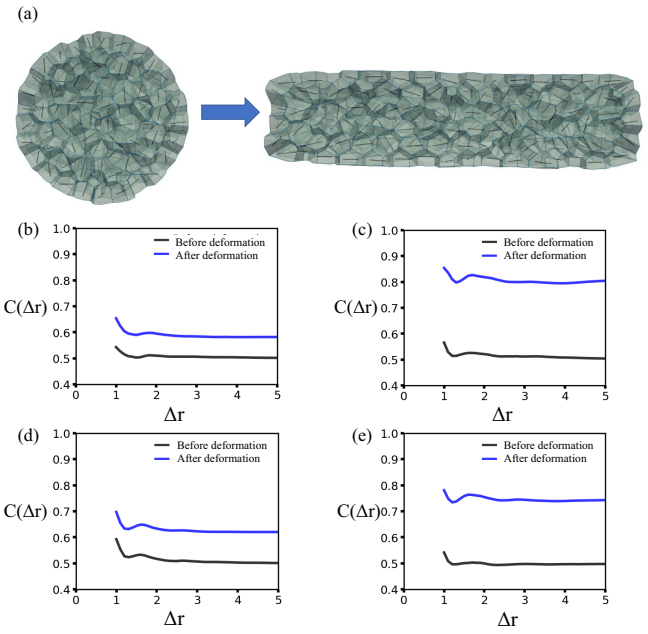

FIG. 3. Boundary-bulk morphology with lateral extensile deformation. (a) Cross-sectional snapshots of the cellular collective before and after the lateral extensile deformation, where the black-colored rods indicate the orientation of cells. [(b)–(e)] The correlation function $C(\Delta r)$ as a function of the distance Δr between the centers of two cells before and after the lateral extensile deformation for (b) bulk cells with $s_0 = 5.6$; (c) boundary cells with $s_0 = 5.6$; (d) bulk cells with $s_0 = 5.0$; and (e) boundary cells with $s_0 = 5.0$.

sharp, but deformable, boundary between two groups of cells distinguished solely by an interfacial line tension between them [49]. More specifically, a discontinuity in the restoring force once a cell has "invaded" the territory of the other group of cells was determined [49]. More recent work with three-dimensional Voronoi models demonstrates that there is an energetic barrier to destabilizing the interface between two cells types within a layered geometry and that within a two cell layer geometry, the centers of the cells align [50]. Here, we observe that the boundary cells are rather responsive to the deformation along with smoothly connected boundary faces given the interfacial surface tension. However, their inner faces can take on a more jagged surface in the absence of an inner interfacial surface tension between the boundary cells and the second inner layer of cells. With this more jagged surface, the interior cells remain insulated, or topologically protected, from deformations at the surface. Note that this behavior is also distinct from earlier work in which a bulk two-dimensional vertex model undergoes pure shear, which results in alignment of the cells [51]. Here, we allow the faces of the system to deform such the overall cellular collective shape is not constrained and includes curvature such that the cells take on a more varied zoology of shapes beyond the one-sided right prism [50]. Moreover, the difference in organization between the boundary cells and the bulks cells persists for faster deformations, though the difference decreases particularly for the fluid-like case (see Fig. S6 within the Supplemental Material [47]).

As for the rheology in response to the deformation, we find the distribution of the shape index of individual cells broadens for both the fluid-like case and the solid-like case, particularly amongst the boundary cells (see Fig. S7 within the Supplemental Material [47]). Interestingly, for the solid-like case, the cell shape index for the boundary cells becomes more broad than for the fluid-like case as the bulk cannot reorganize in response to the deformation, and so the boundary cells remodel even more so in response. In both cases, the enhancement of the cell shape index, particularly in the boundary cells, is due to a decrease in the volume. Variations in the relative stiffnesses of K_A and K_V will modulate this response with a larger K_V resulting in more changes in surface area than in volume of the boundary cells.

In the solid-like system with $s_0 = 5.0$, the decrease in alignment correlation from the boundary to the bulk decreases as the magnitude of the additional surface tension of boundary cells γ is decreased to $\gamma = 0.5$, and increases as γ is increased to $\gamma = 2.0$ (see Fig. S8 within the Supplemental Material [47]). Due to fewer reconnection events in the solid-like phase, an increase in γ leads to more volume shrinkage of boundary cells than the bulk cells, that is a larger volume difference between boundary and bulk cells. As a result of the larger volume difference along with a larger surface tension difference between the outer and inner faces of the boundary cells, the bulk-boundary difference in alignment correlation is enhanced. Similarly, a decrease in the cell volume stiffness K_V leads to larger (boundary surface tension induced) volume shrinkage of boundary cells, so that the bulk-boundary difference in alignment correlation increases (see Fig. S9 within the Supplemental Material [47]). However, in the fluid-like system with $s_0 = 5.6$, with more reconnection events, both boundary and bulk cells experience volume shrinkage together due to an increase in γ, so the bulk-boundary difference in alignment correlation will not increase. Moreover, while the average volume of bulk cells is further decreased, the target surface area of each bulk cell is still $A_0 = 5.6$. Hence the bulk cells intend to have an elongated shape to meet the target surface area, which results in a slight increase in alignment correlation. The decrease in alignment correlation from the boundary to the bulk in fluid-like system also shows a different trend than the solid-like system as K_V is varied. An increase in K_V leads to less volume change but more surface area change in bulk cells, so the bulk cells are able to reconfigure their shapes more freely during later extension, that is a lower alignment correlation and a larger decrease in alignment correlation from the boundary to the bulk.

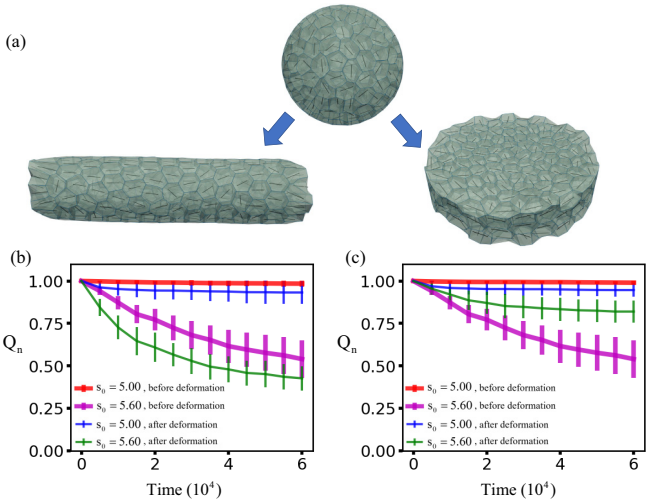

FIG. 4. Rheology response to deformation. (a) Snapshots of the cellular collective before and after the lateral and radial extension, where the black-colored rods indicate the orientation of cells. [(b),(c)] The overlap function Q_n of the bulk cells as a function of simulation time with $s_0 = 5.0, 5.6$, before and after (b) lateral extension and (c) radial extension.

One might initially surmise that with the increase in the individual cell shape index, the cell collective becomes more fluid-like in response to the deformation in both cases. However, with more of the changes occurring in the boundary cells, some of which were initially bulk cells at the start of the deformation, it is not clear. Measurements of the overlap function indicate that for $s_0 = 5.6$, the cellular collective does not become more fluid-like with similar decay of the overlap function Q_n (as a function of time) before and after the deformation. See Figs. 4(a) and 4(b). Moreover, for $s_0 = 5.0$, there also does not appear to be enhanced fluidization of the system. This finding is consistent with the bulk of the cells remaining topologically protected from the deformations at the boundary. However, it would be interesting to determine if the shear thinning observed in a bulk two-dimensional system [52] occurs here.

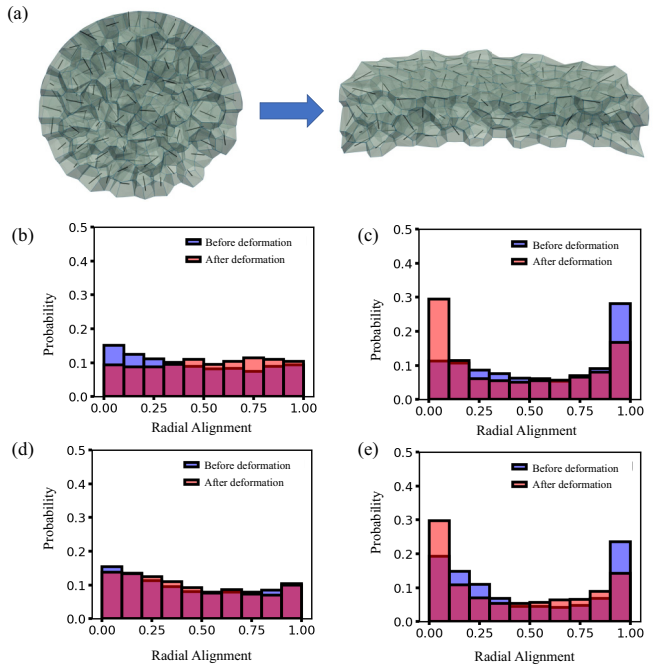

FIG. 5. Boundary-bulk morphology with in-plane, radial extension. (a) Cross-sectional snapshots of the cellular collective before and after the radial extension, where the black-colored rods indicate the orientation of cells. [(b)–(e)] The distribution of $\eta_i(\mathbf{r})$ before and after the in-plane, radial extension for (b) bulk cells with $s_0 = 5.6$; (c) boundary cells with $s_0 = 5.6$; (d) bulk cells with $s_0 = 5.0$; and (e) boundary cells with $s_0 = 5.0$.

C. Boundary-bulk morphology with in-plane, radial extensile strain

Now that we have analyzed the confluent cellular collective's response to lateral, extensile strain, we explore its response to in-plane, radial extensile strain. Given the sharp boundary patterning in the prior case, we expect the bulk cells to neither align in some arbitrary direction. We find that the nematic alignment correlation function for the bulk cells behaves similarly to the lateral extensile deformation. In other words, there is little alignment in the bulk. Given the radial geometry, however, one may anticipate other types of structural ordering, such as those observed in liquid crystals. For instance, splay or $S_i(\mathbf{r}) = \frac{|\vec{\nabla}\cdot\vec{d}_i(\mathbf{r})|^2}{|\vec{d}_i(\mathbf{r})|^2}$ may be relevant. Again, the denominator is present since $\vec{d}_i(\mathbf{r})$ differs in length from cell to cell. While there is very recent work quantifying two-dimensional vertex models as p-actic liquid crystals [28], we will take a simpler approach. We compute for each cell,

$$\eta_i(\mathbf{r}) = |\cos(\theta_i(\mathbf{r}))| = \frac{|\vec{n}_\mathbf{r}\cdot\vec{d}_i(\mathbf{r})|}{|\vec{d}_i(\mathbf{r})|}. \tag{5}$$

and plot the distribution of angles $|\cos\theta_i(\mathbf{r})|$. Here $\vec{n}_\mathbf{r} = \mathbf{r}/|\mathbf{r}|$. Should $|\cos(\theta_i(\mathbf{r})| \approx 0$ then the cells exhibit more curl than splay; should $|\cos(\theta_i(\mathbf{r})| \approx 1$, then the cells exhibit more splay than curl. Note that it is easier to compute $|\theta_i(\mathbf{r})|$ than the curl due to numerical inaccuracies. See Fig. 5. We find that before the deformation, splay is maximized at the boundary for both $s_0 = 5.6$ and $s_0 = 5.0$. However, after the deformation, the boundary cells are oriented circumferentially to exhibit curl. On the other hand, the orientation of the bulk with respect to the radial direction does not change significantly. So, again, with this alternate type of deformation, we observe a boundary-bulk patterning in which the interior cells remain topologically protected (see Movie S2 within the Supplemental Material [47]). Note that the patterning is different than those observed in quasi-two-dimensional brain organoids, where the boundary cells were oriented radially [5]. Bulk cells are indeed moving to the boundary as the deformation occurs, but given the deformation rate, bulk cells are not moving to the boundary fast enough. Should more bulk cells move to the boundary during the deformation, we hypothesize that the boundary cells may become oriented radially. In addition, the boundary-bulk patterning persists for faster deformation rates, while smaller interfacial surface tensions, it is not as robust.

We also investigate how the confluent cellular collective rheology is in response to the in-plane, radial extensile deformation. We observe similar trends as in the lateral extension case in which the solid-like system remains solid-like in terms of the overlap function after the extension. However, for the fluid-like case, the system becomes more solid-like. Intriguingly, this result appears to be in-line with earlier work demonstrating compression-induced fluidization such that one might expect extension-induced solidification [42]. Presumably, the bulk cells in the cortex-core structure for the quasi-two-dimensional brain organoids are also somewhat solid-like [5]. Changes in the cell shape index distribution before and after the deformation appear to be similar to the lateral extension, despite the change in rheology in the fluid-like case to become more solid-like (see Fig. S10 within the Supplemental Material [47]). Again, much of the changes in shape index are focused at the boundary of the confluent cellular collective.

IV. DISCUSSION

We construct and study a three-dimensional vertex model with a quadratic energy functional in terms of a target surface area and a target volume using over-damped Brownian dynamics simulations. In doing so, we uncover a rigidity transition in the bulk system with periodic boundary conditions. By measuring a discrete neighbor overlap function, we determine the transition location to occur at a target shape index of $s_0^* = 5.39 \pm 0.01$, for the system sizes and temperatures studied. This transition location is slightly lower than the location of the rigidity transition observed in a three-dimensional Voronoi version, where the degrees of freedom are assigned to the cell centers, using energy minimization [36]. Density-independent fluidization occurs as isotropic contractility decreases so that anisotropic contractility via stress fibers may ultimately drive cell motion. Such an effect in single cells has been recently emphasized [39] and is likely to occur at the multicellular level [53].

We have also gone beyond a bulk system to examine confluent cellular collectives and their response to deformations. We indeed observe vestiges of the rigidity transition in the confluent cellular collective case. For both lateral and in-plane radial extension, we observe larger changes in the patterning before and after the deformation for the fluid case. Specifically, the change in the nematic-like, or curl-like, alignment,

of the boundary cells is greater in the fluid case. Specifically, for the lateral extension, the cells align with the direction of the extension, while for in-plane radial extension, the boundary cells align perpendicularly to the radial direction. Importantly, there is a significant difference between the bulk cells and the boundary cells in terms of arrangement for both types of deformations. In particular, the bulk cells resemble the cells in the bulk system with periodic boundary conditions, as if there were no boundary deformation at all. In other words, the bulk cells are topologically protected from deformations at the boundary.

As for existing numerical evidence for a boundary-bulk effect, Finegan *et al.* [54] details a wonderful experiment-theory collaboration addressing how Sidekick drives a particular type of reconnection event in Drosophila during a particular time in its development. While the experimental data seems to focus mostly on the bulk, an image of a two-dimensional vertex model simulation with a boundary shows the cells at the boundary do appear to more aligned with respect to each other as compared to alignment in the bulk. As for experimental evidence for a boundary-bulk effect, we refer to an image of the presomitic mesoderm of zebrafish embryo in Mongera *et al.* [55]. While the boundary in the image is not between cells and "empty space" (fluid), but between effectively two different types of cells, ones that are thicker and ones that thinner, such that there is interfacial tension between the two types. In the thicker cells, one observes a top, boundary row of very prism-like cells and just below this top, boundary row, the cells are not prism-like and not very ordered. In other words, there exists some experimental evidence for the boundary-bulk effect, although such an effect needs to be carefully quantified experimentally.

The stark difference between the bulk and boundary cells is a phenomenon that cannot be readily captured in a continuum model. The topologically-protected interior is a consequence of the absence of any interfacial surface tension at the inner faces of the boundary cells. And while there are other ways to depict three-dimensional cellular collectives, such as cellular Potts model [56] or a three-dimensional Voronoi model [36,57], the three-dimensional vertex model is our model of choice. In a recent theoretical study on cell extrusion in planar epithelial [58], 3D vertex model is shown to be capable of modeling scutoids-like packing of epithelia [59] with an extra vertex appearing along the apico-basal axis. Moreover, the overall shape of the confluent cellular collective is deformable. With these features, the cells can take on a more varied zoology of shapes beyond right prisms observed a two-layered, two cell-type Voronoi model with interfacial surface tension between the two cell types [50]. In terms of timescales, at least over time scales larger than the time scale for cellular rearrangements, the boundary cells are indeed insulating the bulk cells from the boundary deformation as the confluent cellular collective deforms. Over shorter times, the shape of the cells mimic the boundary deformation, just as an elastic solid. One can therefore observe in a developmental system, for instance, different regimes of deformations at the cell scale in Drosophila epithelial morphogenesis [54].

The single-cell-layer thick boundary effects provide a mechanism for patterning with a confluent cellular collective in which its interior remains topologically protected from deformations at the boundary. For instance, quasi-two-dimensional brain organoids have a cortex that is approximately one-cell layer thick [5]. And while in our system, the cells orient circumferentially at the boundary after in-plane, radial extension, modulation of strain rate and deformation protocol may effect the orientation of the cells at the boundary. We leave this for future work. If we can understand the mechanisms behind structure formation in organoids, more generally, we can better control their formation so that it becomes more "deterministic". This cell-based approach can then ultimately be used to recapitulate more complex organoid structures, such an octopus-like brain with a core brain and its eight mini brains [60]. While evolution has selected for structures that optimize for specific functions given physical constraints, we can ultimately design brain organoid morphologies, for example, that will allow us to probe the intricate structure-function relationship at the multicellular scale.

Even with this simple confluent cellular collective model that does not investigate additional types of interactions between cells such as polarized tension [33,48], we observe nontrivial phenomenon. It would be interesting to include cell growth, the opening of holes [27], polarized interactions between cells [33,48], and strain-dependent tension remodeling [61,62]. Moreover, with cell growth in a confined, but deformable, environment, such as Matrigel, compressive deformations also may arise. But before building too complex a model, which is typically done to recapitulate experiments, we must first understand the most minimal models at hand, as they themselves can exhibit rich behaviors that the biology has discovered long before our own brains have.

The data that support the findings of this study are available upon request.

ACKNOWLEDGMENTS

We acknowledge discussion with Tara Finegan, Sarthak Gupta, Lisa Manning, and Paula Sanematsu. J.M.S. acknowleges financial support from Grant No. NSF-PoLS-2014192. We also acknowledge helpful feedback from an anonymous reviewer. T.Z. and J.M.S. conceived the study; T.Z. wrote the code and conducted the simulations; T.Z. and J.M.S. interpreted the results and wrote the paper. The authors declare no competing financial or nonfinancial interests.

[1] M. A. Lancaster and J. A. Knoblich, Organogenesis in a dish: Modeling development and disease using organoid technologies, Science **345**, 1247125 (2014).

[2] H. Clevers, Modeling development and disease with organoids, Cell **165**, 1586 (2016).

[3] M. A. Lancaster and J. A. Knoblich, Generation of cerebral organoids from human pluripotent stem cells, Nat. Protocols **9**, 2329 (2014).

[4] M. Hofer and M. P. Lutolf, Engineering organoids, Nat. Rev. Mater. **6**, 402 (2021).

[5] E. Karzbrun, A. Kshirsagar, S. R. Cohen, J. H. Hanna, and O. Reiner, Human brain organoids on a chip reveal the physics of folding, Nat. Phys. **14**, 515 (2018).

[6] M. A. Lancaster, M. Renner, C.-A. Martin, D. Wenzel, L. S. Bicknell, M. E. Hurles, T. Homfray, J. M. Penninger, A. P. Jackson, and J. A. Knoblich, Cerebral organoids model human brain development and microcephaly, Nature (London) **501**, 373 (2013).

[7] S. Velasco, A. J. Kedaigle, S. K. Simmons, A. Nash, M. Rocha, G. Quadrato, B. Paulsen, L. Nguyen, X. Adiconis, A. Regev *et al.*, Individual brain organoids reproducibly form cell diversity of the human cerebral cortex, Nature (London) **570**, 523 (2019).

[8] C. A. Trujillo, R. Gao, P. D. Negraes, J. Gu, J. Buchanan, S. Preiss, A. Wang, W. Wu, G. G. Haddad, I. A. Chaim *et al.*, Complex oscillatory waves emerging from cortical organoids model early human brain network development, Cell Stem Cell **25**, 558 (2019).

[9] T. Sato, R. G. Vries, H. J. Snippert, M. Van De Wetering, N. Barker, D. E. Stange, J. H. Van Es, A. Abo, P. Kujala, P. J. Peters *et al.*, Single Lgr5 stem cells build crypt-villus structures in vitro without a mesenchymal niche, Nature (London) **459**, 262 (2009).

[10] A. Ramani, L. Müller, P. N. Ostermann, E. Gabriel, P. Abida-Islam, A. Müller-Schiffmann, A. Mariappan, O. Goureau, H. Gruell, A. Walker *et al.*, SARS-CoV-2 targets neurons of 3D human brain organoids, EMBO J. **39**, e106230 (2020).

[11] B.-Z. Zhang, H. Chu, S. Han, H. Shuai, J. Deng, Y.-fan Hu, H.-rui Gong, A. C.-Y. Lee, Z. Zou, T. Yau *et al.*, SARS-CoV-2 infects human neural progenitor cells and brain organoids, Cell Res. **30**, 928 (2020).

[12] N. Gjorevski, M. Nikolaev, T. E. Brown, O. Mitrofanova, N. Brandenberg, F. W. DelRio, F. M. Yavitt, P. Liberali, K. S. Anseth, and M. P. Lutolf, Tissue geometry drives deterministic organoid patterning, Science **375**, eaaw9021 (2022).

[13] A. Borzou and J. M. Schwarz, Large-scale cortex-core structure formation in brain organoids, Frontiers Phys. **10**, 837600 (2022).

[14] T. Nagai, S. Ohta, K. Kawasaki, and T. Okuzono, Computer simulation of cellular pattern growth in two and three dimensions, Phase Transit. **28**, 177 (1990).

[15] K. Fuchizaki, T. Kusaba, and K. Kawasaki, Computer modelling of three-dimensional cellular pattern growth, Philos. Mag. B **71**, 333 (1995).

[16] H. Honda, M. Tanemura, and T. Nagai, A three-dimensional vertex dynamics cell model of space-filling polyhedra simulating cell behavior in a cell aggregate, J. Theor. Biol. **226**, 439 (2004).

[17] S. Okuda, Y. Inoue, and T. Adachi, Three-dimensional vertex model for simulating multicellular morphogenesis, Biophys. Physicobiology **12**, 13 (2015).

[18] M. Krajnc, S. Dasgupta, P. Ziherl, and J. Prost, Fluidization of epithelial sheets by active cell rearrangements, Phys. Rev. E **98**, 022409 (2018).

[19] H. Honda, Y. Ogita, S. Higuchi, and K. Kani, Cell movements in a living mammalian tissue: Long-term observation of individual cells in wounded corneal endothelia of cats, J. Morphol. **174**, 25 (1982).

[20] R. Farhadifar, J. C. Röper, B. Aigouy, S. Eaton, and F. Jülicher, The influence of cell mechanics, cell-cell interactions, and proliferation on epithelial packing, Curr. Biol. **17**, 2095 (2007).

[21] D. B. Staple, R. Farhadifar, J. C. Röper, B. Aigouy, S. Eaton, and F. Jülicher, Mechanics and remodelling of cell packings in epithelia, Eur. Phys. J. E **33**, 117 (2010).

[22] A. G. Fletcher, M. Osterfield, R. E. Baker, and S. Y. Shvartsman, Vertex models of epithelial morphogenesis, Biophys. J. **106**, 2291 (2014).

[23] D. Bi, J. H. Lopez, J. M. Schwarz, and M. L. Manning, A density-independent rigidity transition in biological tissues, Nat. Phys. **11**, 1074 (2015).

[24] D. Bi, X. Yang, M. C. Marchetti, and M. L. Manning, Motility-Driven Glass and Jamming Transitions in Biological Tissues, Phys. Rev. X **6**, 021011 (2016).

[25] L. Yan and D. Bi, Multicellular Rosettes Drive Fluid-solid Transition in Epithelial Tissues, Phys. Rev. X **9**, 011029 (2019).

[26] P. Sahu, D. M. Sussman, M. Rübsam, A. F. Mertz, V. Horsley, E. R. Dufresne, C. M. Niessen, M. C. Marchetti, M. L. Manning, and J. M. Schwarz, Small-scale demixing in confluent biological tissues, Soft Matter **16**, 3325 (2020).

[27] S. Kim, M. Pochitaloff, G. A. Stooke-Vaughan, and O. Campàs, Embryonic tissues as active foams, Nat. Phys. **17**, 859 (2021).

[28] J.-M. Armengol-Collado, L. N. Carenza, J. Eckert, D. Krommydas, and L. Giomi, Epithelia are multiscale active liquid crystals, arXiv:2202.00668.

[29] A. G. Fletcher, J. M. Osborne, P. K. Maini, and D. J. Gavaghan, Implementing vertex dynamics models of cell populations in biology within a consistent computational framework, Prog. Biophys. Mol. Biol. **113**, 299 (2013).

[30] G. R. Mirams, C. J. Arthurs, M. O. Bernabeu, R. Bordas, J. Cooper, A. Corrias, Y. Davit, S.-J. Dunn, A. G. Fletcher, D. G. Harvey *et al.*, Chaste: An open source C + + library for computational physiology and biology, PLoS Comput. Biol. **9**, e1002970 (2013).

[31] D. M. Sussman, cellGPU: Massively parallel simulations of dynamic vertex models, Comput. Phys. Commun. **219**, 400 (2017).

[32] D. L. Barton, S. Henkes, C. J Weijer, and R. Sknepnek, Active vertex model for cell-resolution description of epithelial tissue mechanics, PLoS Comput. Biol. **13**, e1005569 (2017).

[33] S. Okuda and K. Sato, Polarized interfacial tension induces collective migration of cells, as a cluster, in a 3D tissue, Biophys. J. **121**, 1856 (2022).

[34] S. Okuda, T. Miura, Y. Inoue, T. Adachi, and M. Eiraku, Combining turing and 3D vertex models reproduces autonomous multicellular morphogenesis with undulation, tubulation, and branching, Sci. Rep. **8**, 2386 (2018).

[35] J.-A. Park, J. H. Kim, D. Bi, J. A. Mitchel, N. T. Qazvini, K. Tantisira, C. Y. Park, M. McGill, S.-H. Kim, B. Gweon *et al.*, Unjamming and cell shape in the asthmatic airway epithelium, Nat. Mater. **14**, 1040 (2015).

[36] M. Merkel and M. L. Manning, A geometrically controlled rigidity transition in a model for confluent 3D tissues, New J. Phys. **20**, 022002 (2018).

[37] J. Rozman, M. Krajnc, and P. Ziherl, Collective cell mechanics of epithelial shells with organoid-like morphologies, Nat. Commun. **11**, 3805 (2020).

[38] B. D. Hoffman and A. S. Yap, Towards a dynamic understanding of cadherin-based mechanobiology, Trends Cell Biol. **25**, 803 (2015).

[39] E. Warmt, S. Grosser, E. Blauth, X. Xie, H. Kubitschke, R. Stange, F. Sauer, J. Schnauß, J. M. Tomm, M. von Bergen *et al.*, Differences in cortical contractile properties between healthy epithelial and cancerous mesenchymal breast cells, New J. Phys. **23**, 103020 (2021).

[40] S. Okuda, Y. Inoue, M. Eiraku, Y. Sasai, and T. Adachi, Reversible network reconnection model for simulating large deformation in dynamic tissue morphogenesis, Biomech. Model. Mechanobiol. **12**, 627 (2013).

[41] C. H. Rycroft, VORO + +: A three-dimensional Voronoi cell library in C + +, Chaos **19**, 041111 (2009).

[42] A. Parker, M. C. Marchetti, M. L. Manning, and J. M. Schwarz, How does the extracellular matrix affect the rigidity of an embedded spheroid? arXiv:2006.16203.

[43] C. Abaurrea-Velasco, T. Auth, and G. Gompper, Vesicles with internal active filaments: Self-organized propulsion controls shape, motility, and dynamical response, New J. Phys. **21**, 123024 (2019).

[44] F. Giavazzi, M. Paoluzzi, M. Macchi, D. Bi, G. Scita, M. L. Manning, R. Cerbino, and M. C. Marchetti, Flocking transitions in confluent tissues, Soft Matter **14**, 3471 (2018).

[45] A. Das, S. Sastry, and D. Bi, Controlled Neighbor Exchanges Drive Glassy Behavior, Intermittency, and Cell Streaming in Epithelial Tissues, Phys. Rev. X **11**, 041037 (2021).

[46] G. Erdemci-Tandogan and M. Lisa Manning, Effect of cellular rearrangement time delays on the rheology of vertex models for confluent tissues, PLoS Comput. Biol. **17**, e1009049 (2021).

[47] See Supplemental Material at http://link.aps.org/supplemental/10.1103/PhysRevResearch.4.043148 for shape index distribution for the bulk system for different target shape indices, overlap function with extended definitions, alignment correlation function for bulk cells, alignment correlation function for outermost layer and second outer layer, cell aspect ratio distributions before and after the lateral extensile deformation, alignment correlation function with higher lateral extensile deformation speed, cell shape index and volume distributions before and after the lateral extensile deformation, alignment correlation function for different values of boundary cell surface tension stiffness, alignment correlation function for different values of cell volume stiffness, cell shape index and volume distributions before and after the radial extensile deformation, movie for the lateral extensile deformation of the cellular collective, and movie for the radial extensile deformation of the cellular collective.

[48] J. Comelles, S. S. Soumya, L. Lu, E. Le Maout, S. Anvitha, G. Salbreux, F. Jülicher, M. M. Inamdar, and D. Riveline, Epithelial colonies in vitro elongate through collective effects, Elife **10**, e57730 (2021).

[49] D. M. Sussman, J. M. Schwarz, M. C. Marchetti, and M. L. Manning, Soft yet Sharp Interfaces in a Vertex Model of Confluent Tissue, Phys. Rev. Lett. **120**, 058001 (2018).

[50] P. Sahu, J. M. Schwarz, and M. L. Manning, Geometric signatures of tissue surface tension in a three-dimensional model of confluent tissue, New J. Phys. **23**, 093043 (2021).

[51] X. Wang, M. Merkel, L. B Sutter, G. Erdemci-Tandogan, M. L. Manning, and K. E. Kasza, Anisotropy links cell shapes to tissue flow during convergent extension, Proc. Natl. Acad. Sci. U.S.A. **117**, 13541 (2020).

[52] C. Duclut, J. Paijmans, M. M. Inamdar, C. D. Modes, and F. Jülicher, Nonlinear rheology of cellular networks, Cells Dev. **168**, 203746 (2021).

[53] O. Ilina, P. G. Gritsenko, S. Syga, J. Lippoldt, C. A. M. La Porta, O. Chepizhko, S. Grosser, M. Vullings, G.-J. Bakker, J. Starruß *et al.*, Cell–cell adhesion and 3D matrix confinement determine jamming transitions in breast cancer invasion, Nat. Cell Biol. **22**, 1103 (2020).

[54] T. M. Finegan, N. Hervieux, A. Nestor-Bergmann, A. G. Fletcher, G. B. Blanchard, and B. Sanson, The tricellular vertex-specific adhesion molecule sidekick facilitates polarised cell intercalation during drosophila axis extension, PLoS Biol. **17**, e3000522 (2019).

[55] A. Mongera, P. Rowghanian, H. J. Gustafson, E. Shelton, D. A. Kealhofer, E. K. Carn, F. Serwane, A. A. Lucio, J. Giammona, and O. Campàs, A fluid-to-solid jamming transition underlies vertebrate body axis elongation, Nature (London) **561**, 401 (2018).

[56] R. Chaturvedi, C. Huang, B. Kazmierczak, T. Schneider, J. A. Izaguirre, T. Glimm, H. G. E. Hentschel, J. A. Glazier, S. A. Newman, and M. S. Alber, On multiscale approaches to three-dimensional modelling of morphogenesis, J. R. Soc. Interface **2**, 237 (2005).

[57] S. Grosser, J. Lippoldt, L. Oswald, M. Merkel, D. M. Sussman, F. Renner, P. Gottheil, E. W. Morawetz, T. Fuhs, X. Xie, S. Pawlizak, A. W. Fritsch, B. Wolf, L. C. Horn, S. Briest, B. Aktas, M. L. Manning, and J. A. Kas, Cell and Nucleus Shape as an Indicator of Tissue Fluidity in Carcinoma, Phys. Rev. X **11**, 011033 (2021).

[58] S. Okuda and K. Fujimoto, A mechanical instability in planar epithelial monolayers leads to cell extrusion, Biophys. J. **118**, 2549 (2020).

[59] P. Gómez-Gálvez, P. Vicente-Munuera, A. Tagua, C. Forja, A. M. Castro, M. Letrán, A. Valencia-Expósito, C. Grima, M. Bermúdez-Gallardo, Ó. Serrano-Pérez-Higueras *et al.*, Scutoids are a geometrical solution to three-dimensional packing of epithelia, Nat. Commun. **9**, 2960 (2018).

[60] B. Hochner, An embodied view of octopus neurobiology, Curr. Biol. **22**, R887 (2012).

[61] M. F. Staddon, K. E. Cavanaugh, E. M. Munro, M. L. Gardel, and S. Banerjee, Mechanosensitive junction remodeling promotes robust epithelial morphogenesis, Biophys. J. **117**, 1739 (2019).

[62] K. E. Cavanaugh, M. F. Staddon, E. Munro, S. Banerjee, and M. L. Gardel, RhoA mediates epithelial cell shape changes via mechanosensitive endocytosis, Dev. Cell **52**, 152 (2020).